CrossMark

Structural, dielectric and AC conductivity studies of Zn substituted nickel ferrites prepared by combustion technique

G. Umapathy[1] · G. Senguttuvan[1] · L. John Berchmans[2] · V. Sivakumar[1]

Abstract A series of zinc doped nickel ferrites having the chemical formula $Ni_{1-x}Zn_xFe_2O_4$ [x = 0.0, 0.25, 0.50, 0.75, 1.0] were synthesized by combustion method. The powder X-ray diffraction results confirm the formation of single phase cubic spinel structure. The lattice parameter was found to increase from 8.348 to 8.443 Å with increase in the Zn content. Average crystallite size calculated using Debye–Scherrer equation and Williamson–Hall plots confirms the nano crystalline nature of the samples. The EDAX analysis indicates the correct elemental composition of the synthesized powders. Fourier transform infrared spectra show the characteristic peaks of Ni–Zn spinel ferrites. The morphological features of the powder were examined by SEM and reveal the fine crystalline nature of the powder. A systematic study on the dielectric properties such as dielectric constant (ε'), dielectric loss tangent (tan δ) and AC conductivity (σ_{ac}) were investigated as a function of Zn content and frequency in the range from 100 Hz to 1 MHz at room temperature. Complex impedance behavior was explained by means of the cole–cole plot.

1 Introduction

Nanosized spinel ferrite particles with structural formula of MFe_2O_4 (M = divalent metal ion) have been investigated in the recent years by many researchers, due to their unique electric, dielectric and magnetic properties. It is observed that the properties of ferrites strongly depend upon many factors including the method of preparation, composition of constituents, grain structure or size and the amount and type of substitution [1]. Several novel synthesis methods [2–8] have been proposed to synthesize nickel based ferrite nano-particles. Selection of suitable method is the key factor to obtain ferrites with high quality, especially for those with low loss at high frequency [9]. In the present investigation, combustion method has been selected as a novel and energy-efficient technique for the synthesis of nanosized Ni–Zn ferrite materials because of its advantages such as: the homogeneous distribution of ions at the molecular level, good control of stoichiometry and production of ultrafine particles with narrow size distribution in a relatively short processing time at a very low temperature. Further, Urea (NH_2CONH_2) has become an attractive fuel for the preparation of nano powders with crystallite sizes in nanometer range and act as a complexing agent for metal ions because it contains two amino groups located at the extremes of its chemical structure. Nitrates are chosen as metal precursors because of their higher water solubility and for allowing greater homogenization.

The properties of Zn-substituted nickel ferrites have attracted considerable attention because of the importance of these materials as high frequency ferrites for power transformer core, rod antennas, RF coil and radar-absorbing materials (RAM) [10, 11]. Yan et al. [12] have synthesized monodisperse Ni–Zn ferrites ($Ni_xZn_{1-x}Fe_2O_4$)

✉ G. Senguttuvan
sengutuvan@yahoo.com

[1] Department of Physics, Anna University Chennai-BIT Campus, Tiruchirappalli, Tamil Nadu 620024, India

[2] Electropyrometallurgy Division, CSIR-Central Electrochemical Research Institute, Karaikudi 630 006, India

microspheres via solvothermal method and reported the application of these materials in bionanoscience and electronic devices technology. They also reported that $Ni_{0.2}Zn_{0.8}Fe_2O_4$ microspheres could reach maximum magnetic saturation value of 60.6 emu/g. Sreeja et al. [13] reported the magnetic and Mössbauer spectroscopic studies of Ni–Zn ferrite nanoparticles synthesized by a combustion method. They obtained higher Curie temperatures for the nanosized powders when compared to that in the bulk. This was due to the difference in the distribution of the cations in the tetrahedral and octahedral sites of the spinel lattice. Saafan et al. [14] have investigated ac and dc conductivity of Ni–Zn ferrites in wet and dry conditions. The behavior of conductivity differs significantly in these two conditions showing a noticeable effect due to humidity. Ramakrishna et al. [15] have prepared a series of Ni–Zn ferrites with composition $Ni_{1-x}Zn_xFe_2O_4$ where x = 0.0 to 1.0 by citrate precursor method. They observed that Curie temperature and activation energy decreases from x = 0.0 to 1.0, whereas the DC resistivity increases gradually from nickel to zinc ferrite. Min Zhang et al. [16] have studied size effects on magnetic properties of $Ni_{0.5}Zn_{0.5}Fe_2O_4$ powder. They found that the saturation magnetization increases with increasing particle size, which can be explained on the basis of cation distribution in tetrahedral and octahedral sites and due to domain wall movement. Hajalilou et al. [17]. synthesized $Ni_{0.64}Zn_{0.36}Fe_2O_4$ nanoparticles by high-energy milling and subsequent annealing treatment. They reported a saturation magnetization of 5 emu/g for 30 h milled sample which increased to 16 emu/g after annealing was done at 400 °C. However, it was hard to find the studies on the effect of Zn content on structural and dielectric properties of Ni–Zn ferrite. In view of the above, the present study focuses on the synthesis of Ni–Zn ferrites using combustion method and investigates their structural, dielectrics and AC conductivity in detail.

2 Experimental procedure

Nanosized samples of $Ni_{1-x}Zn_xFe_2O_4$ (x = 0.0, 0.25, 0.50, 0.75 and 1.0) were synthesized using nickel nitrate[$Ni(NO_3)_2 \cdot 6H_2O$], zinc nitrate [$Zn(NO_3)_2 \cdot 6H_2O$], and iron nitrate [$Ni(NO_3)_3 \cdot 9H_2O$)], and urea [(NH_2CONH_2)] to serve as a fuel. Stoichiometric proportion of these chemicals were weighed and dissolved in de-ionized water to form solution. The mixed solution was taken in a quartz bowl and stirred for 2 h to obtain a homogeneous viscous solution. Then the bowl was placed on a hotplate and heated to 300 °C to initiate self propagating exothermic reaction evolving large amount of gases. The gas evolution was followed by frothing and swelling of the resultant powder, resulting with the desired ferrites in the form of foamy powders [18]. The synthesized powders were finely grounded and calcinated at 800 °C for 5 h in air by keeping the product in an electrical resistance furnace. For the purpose of dielectric study, the required quantity of powders were mixed with 5 wt% polyvinyl alcohol and made into pellets. The pelletisation was done using a die set and a hand operated hydraulic press at a pressure of 200 kg/cm^2.

3 Characterization

X-ray powder diffraction (XRD) analysis was carried out using X-ray powder diffractometer (BRUKER D8 ADVANCED) with Cu Kα radiation (λ = 1.5406 Å). The FTIR measurements were made with Perklin Elmer UK paragon-500 spectrophotometer in the mid infrared region (4000–400 cm^{-1}). The elemental analysis of the powders was done using the Energy Dispersive X-ray analysis (EDAX) technique. The morphological features of the synthesized nano powders were analyzed using JEOL-JSM-3.5CF instrument. The dielectric studies were measured in the frequency range of 100 kHz to 1 MHz using LCR Hi- Tester (Hioki 3532-56).

## 4 Results and discussion

4.1 Structural properties

4.1.1 X-ray diffraction

XRD profiles of the $Ni_{1-x}Zn_xFe_2O_4$ (x = 0, 0.25, 0.5, 0.75 and 1.0) samples are shown in Fig. 1a. The XRD patterns confirm the formation of spinel cubic structure with Fd3 m space group, which is consistent with standard JCPDS: (86-2267) files. The broadening of the diffraction lines ascertains the nanocrystallinity of the synthesized powders. The spectra exhibit the crystalline nature of the samples with no extra peaks noticed in the spectrum which reveals the absence of any unreacted constituents in the synthesized compounds. Figure 1b shows the magnified XRD peaks located in the vicinity of 2θ = 35.5° corresponding to (311) plane for pure and Zn-doped nickel ferrite. The lower angle shift in the XRD peaks of Zn-doped nickel ferrite nanoparticles indicates the replacement of Ni^{2+} ions by Zn^{2+} ions.

The X-ray density (ρ_x) of the samples was calculated using the expression given by Smit and Wijn [19]:

$$\rho_x = \frac{nM}{N_A a^3} \tag{1}$$

Fig. 1 a X-ray diffraction analysis of Zn doped nickel ferrite. **b** Dopant induced peak shift (311) due to incorporation of Zn
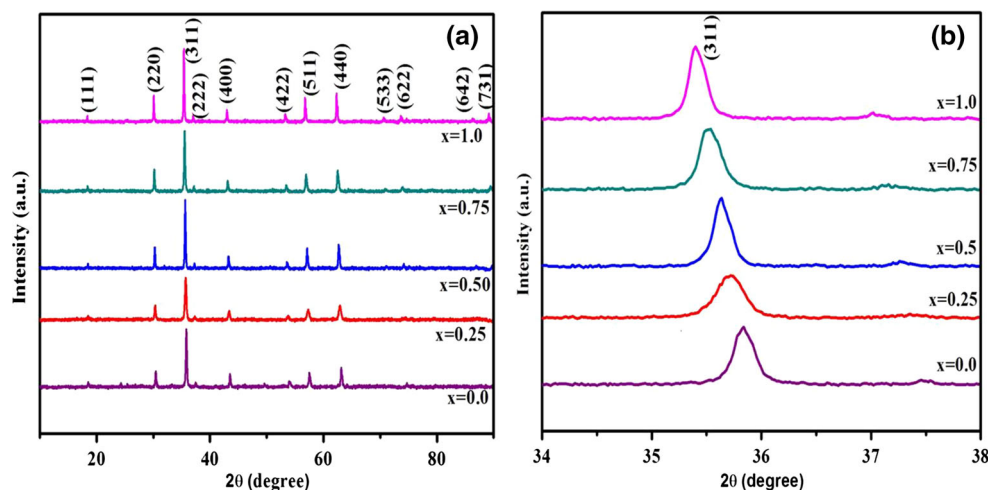
where M, N_A, n and a are the molecular weight of the samples, Avogadro's number (6.0225×10^{23} atom/mol), number of formula unit present in a unit cell (in the present case, $n = 8$) and the lattice parameter respectively. Figure 2 shows the variation of ρ_x as a function of Zn content. It is shown that ρ_x decreases with increasing Zn content in nickel ferrite. The value of ρ_x for $NiFe_2O_4$ was found to be 5.435 g/cm^3, while it was 5.402 g/cm^3 for $ZnFe_2O_4$. The decrease of ρ_x with Zn ion content could be attributed to the atomic weight and the radii of constituent ions.

The average crystallite size of the synthesized powders was determined using Debye–Scherrer's equation [20].

$$D = \frac{k\lambda}{\beta_{hkl} \cos \theta} \tag{2}$$

where, k is the shape factor (k = 0.9), λ is the wavelength of Cu-Kα radiation and β_{hkl} is the instrument corrected
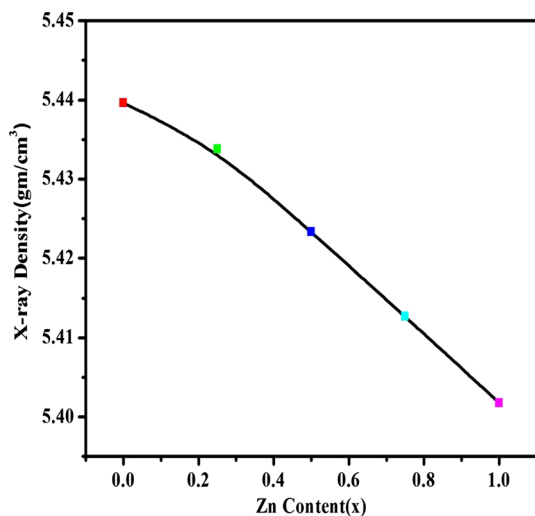
integral breadth of the reflection located at 2θ and θ is the angle of reflection. In order to obtain β_{hkl} of each diffraction peak, a non-linear least square fit has been constructed assuming that the experimentally obtained diffraction peaks obey Lorentzian function. The instrumental corrected integral breadth (β_{hkl}) of the reflection located at 2θ broadening was corrected to each diffraction peaks of Ni–Zn materials using the equation

$$\beta_{hkl} = \left[(\beta_{hkl})^2_{measured} + (\beta_{hkl})^2_{instrumental} \right]^{1/2} \tag{3}$$

The average crystallite size of Ni–Zn ferrites obtained at different concentration of Zn is listed in Table 1.

The strain in the powders due to the contribution of crystal imperfection and distortion can be calculated using the Eq. (4)

$$\varepsilon = \frac{\beta_{hkl}}{4 \tan \theta} \tag{4}$$

Assuming that the crystallite size and strain contribution to line broadening are independent to each other and both have been Cauchy-like profile, the line breadth can be obtained by combining Eqs. (2) and (4). That is,

$$\beta_{hkl} \cos \theta = \frac{k\lambda}{D} + 4\varepsilon \sin \theta \tag{5}$$

The above Eq. (5) is known as Williamson–Hall (W–H) equation.

W–H plots (Fig. 3) are drawn for all the samples with 4sinθ along the x-axis and βcosθ along the y-axis for the peaks of Ni–Zn with varying concentrations of Zn. From the plot, lattice strain and crystallite size are calculated respectively from the slope and y-intercept of the fitted line. The positive slope from the plots indicates the presence of tensile strain in the Ni–Zn cubic system. The micro distortion for the pure and Zn substituted nickel ferrite compounds exhibit a slight increase in values for the higher

Fig. 2 Variation of X-ray density with Zn content

Table 1 Structural parameters of $Ni_{1-x}Zn_xFe_2O_4$ nanoparticles

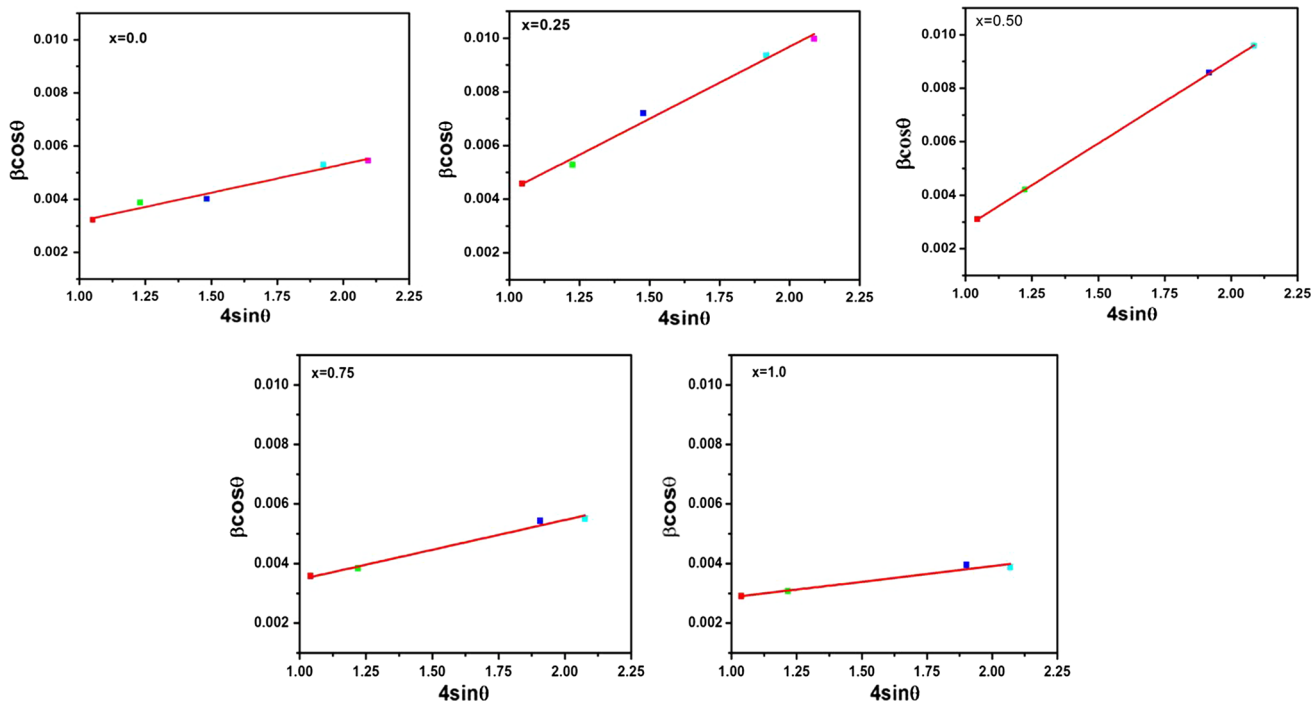| Composition	Crystallite size (nm) by		Lattice parameter (Å)	Strain
	(Scherrer's formula)	(W–H method)		
$NiFe_2O_4$	36	42	8.3053	0.0021
$Ni_{0.75}Zn_{0.25}Fe_2O_4$	26	31	8.3210	0.0054
$Ni_{0.5}Zn_{0.5}Fe_2O_4$	45	50	8.3504	0.0063
$Ni_{0.25}Zn_{0.75}Fe_2O_4$	36	40	8.3754	0.0020
$ZnFe_2O_4$	45	48	8.4005	0.0020

Fig. 3 Williamson–Hall plot for $Ni_{1-x}Zn_xFe_2O_4$ (x = 0.0 to 1.0)

concentration of Zn^{2+} ions. It is also noticed that there is a decrease in micro distortion when the concentrations of Zn^{2+} ions is above x = 0.5. This may be attributed to a change in the cationic distribution in Ni–Zn lattice. The obtained crystallite sizes from W–H plots were compared with the same calculated by the Scherrer equation and are found to be in good agreement. The variation of crystallite size with Zn doping in nickel ferrite is shown in Fig. 4a. It is evident that maximum crystallite size is found when x = 0.5 for $Ni_{1-x}Zn_xFe_2O_4$ samples.

The lattice parameter (*a*) of the synthesized ferrite powders is determined using the formula given below [21]:

$$a = \frac{\lambda}{2} \times \frac{(h^2 + k^2 + l^2)}{\sin \theta} \qquad (6)$$

where (h k l) are the Miller indices, and θ is the diffraction angle corresponding to the (h k l) plane. Figure 4b shows the variation of lattice parameter with increase in concentration of Zn^{2+} ions in the Ni–Zn ferrite system. From the figure it

can be seen that the lattice parameter was found to increase from 8.3053 to 8.4005 Å as 'x' varies from 0.0 to 1.0 in $Ni_{1-x}Zn_xFe_2O_4$. Since ionic radius of both Zn^{2+} (0.82 Å) and Ni^{2+} (0.78 Å) are larger than the interstices of A-site (0.58 Å) and B-site (0.73 Å) in spinel cubic structure, the doping of Zn^{2+} or Ni^{2+} ions into the interstice leads to lattice expansion [22]. However, large expansion of lattice is attributed to the higher doping of Zn^{2+} for Ni^{2+} ions in the nickel ferrite [23]. Thus Ni–Zn ferrite system obeys Vegard's law. A similar variation was also observed by Sorescu [24]. These results suggest the formation of a compositionally homogeneous solid solution of $Ni_{1-x}Zn_xFe_2O_4$.

4.1.2 Fourier transform infrared spectroscopic analysis (FTIR)

The FTIR spectrum elucidates the position of the ions in the crystal lattice and their vibration modes. It can be seen from Fig. 5 that the spectra exhibit two prominent
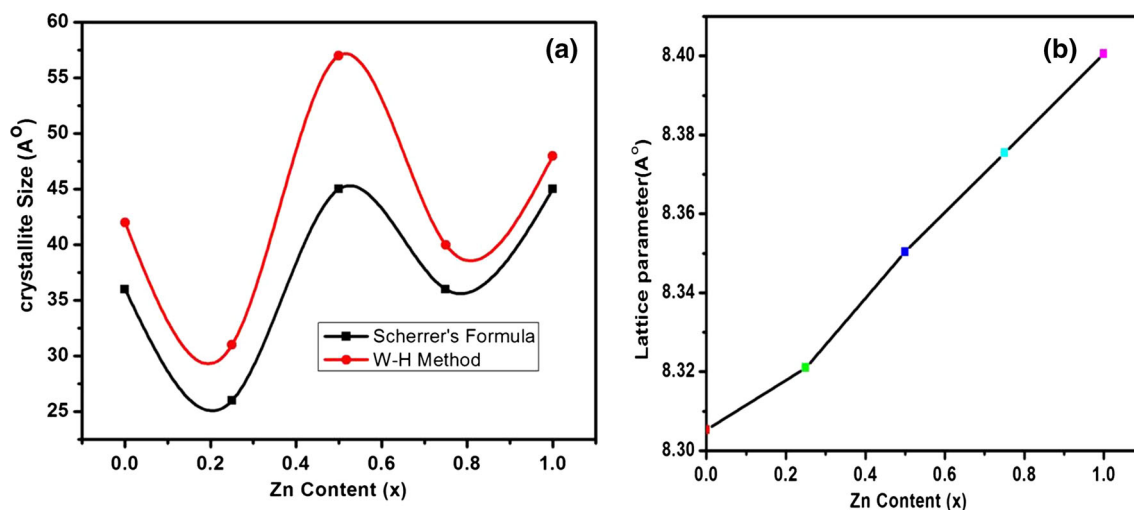
Fig. 4 a Variation of crystallite size with respective to Zn content. **b** Variation of lattice parameter with respective to Zn content for $Ni_{1-x}Zn_xFe_2O_4$ (x = 0.0 to 1.0)

absorption bands in the range 594–565 cm^{-1} (υ_1) and nearer to 422 cm^{-1} (υ_2).

According to Waldron [25], the higher absorption band (υ_1) corresponds to intrinsic stretching vibrations of metal ions at tetrahedral site, ($M_{tetra} \leftrightarrow O$), whereas the lower absorption band (υ_2) corresponds to octahedral-metal stretching ($M_{octa} \leftrightarrow O$). It can be seen that the primary band, υ_1, initially increases from 565 to 594 cm^{-1} and then decrease to 586 cm^{-1} with increasing Zn content, whereas, υ_2, remains unaffected with varying composition. Similar behavior was reported by other researchers [26, 27]. This behavior may be attributed due to the existence of mixed cationic distribution by referring to cationic distribution based Mossbauer studies [28] of similar compositions. The existence of mixed cationic distribution depends on Ni–Zn ratio and other factors. The absorption bands observed around 3440–3436 and 1618–1622 cm^{-1} are due to the presence of moisture (OH^-) on the surface of ferrite

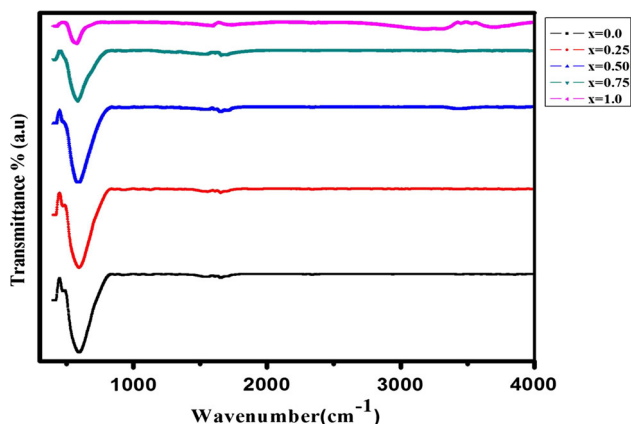nanoparticles. Further, absorption bands around 2318–2324 and 1039–1045 cm^{-1} correspond to atmospheric or absorbed Co_3^{2-} and nitrate ions respectively.

4.2 SEM and EDAX analysis

The morphology of the prepared Ni–Zn ferrite nanoparticles were examined by means of Scanning Electron Microscopy (SEM). Figure 6a shows the SEM photographs of $Ni_{1-x}Zn_xFe_2O_4$ samples for varying values of x (A: x = 0.0, B: x=0.5 and C: x=1.0). It can be seen from the images that the presence of voids and pores on the surface proves that Ni–Zn crystals with enhanced surface area can be produced by solution combustion technique. This manifests in the release of more heat during the combustion reaction, which causes fusion of the Ni–Zn nanoparticles. The samples having multigrain agglomerations consisting of very fine crystallites may be due to magnetostatic interaction of crystallites. The changes in microstructure with varying concentration of Zn^{2+} in nickel ferrite can be seen from the SEM images.

To verify the chemical composition and elemental stoichiometry of the synthesized sample, EDAX analysis of $Ni_{1-x}Zn_xFe_2O_4$ samples (A: x = 0.0, B: x= 0.5 and C: x= 1.0) was done and the spectra are shown in shown in Fig. 6b. The spectra show the presence of elements like Fe, Ni, Zn and O. In the compound, the calculated percentage of Ni/Zn value matches very well with the amount of Ni/Zn used in the respective precursors.

4.3 Dielectric properties

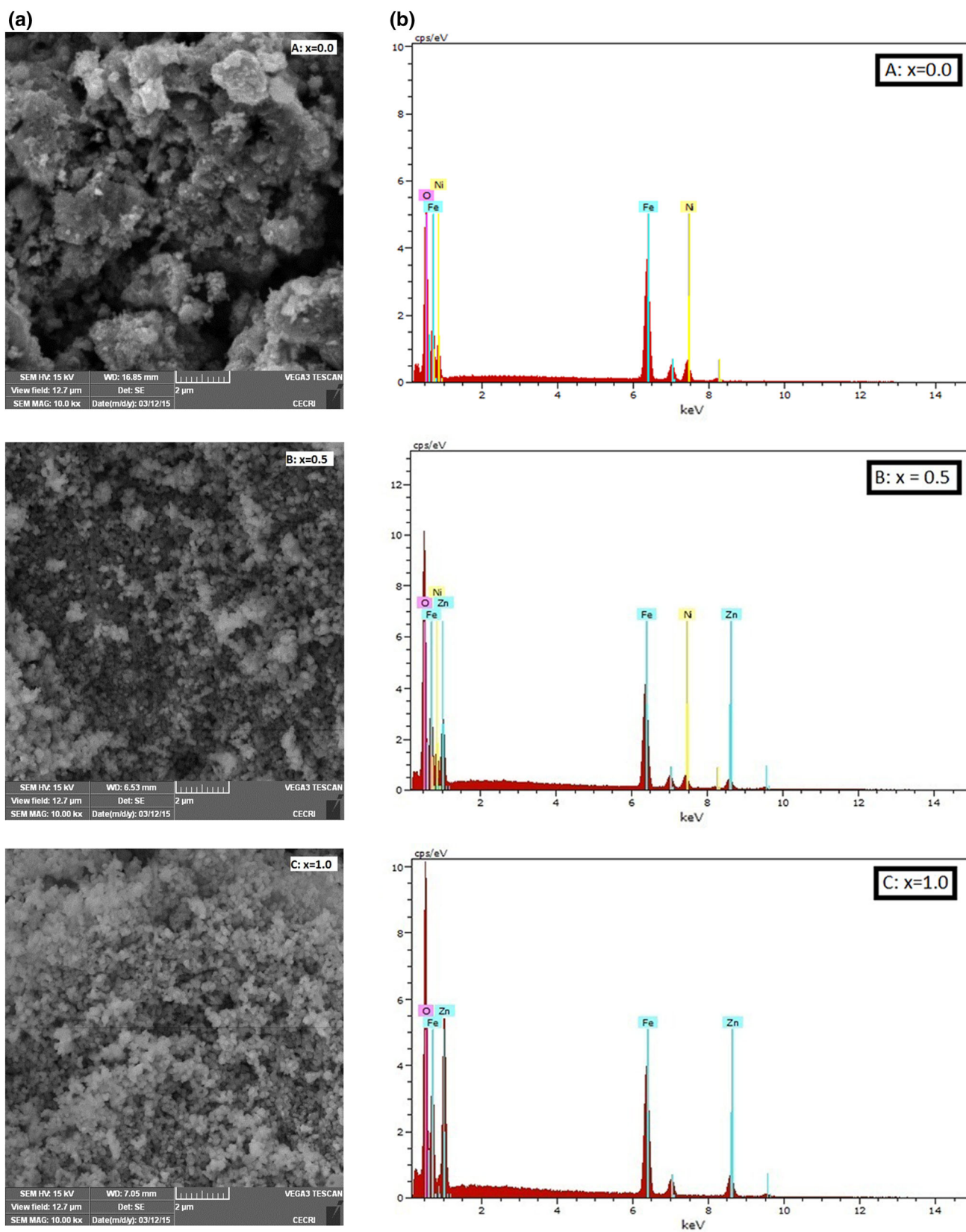The dielectric properties were measured using LCR Hi-Tester in the frequency range 100 Hz–1 MHz at room

Fig. 5 FTIR spectra of $Zn_xNi_{1-x}Fe_2O_4$

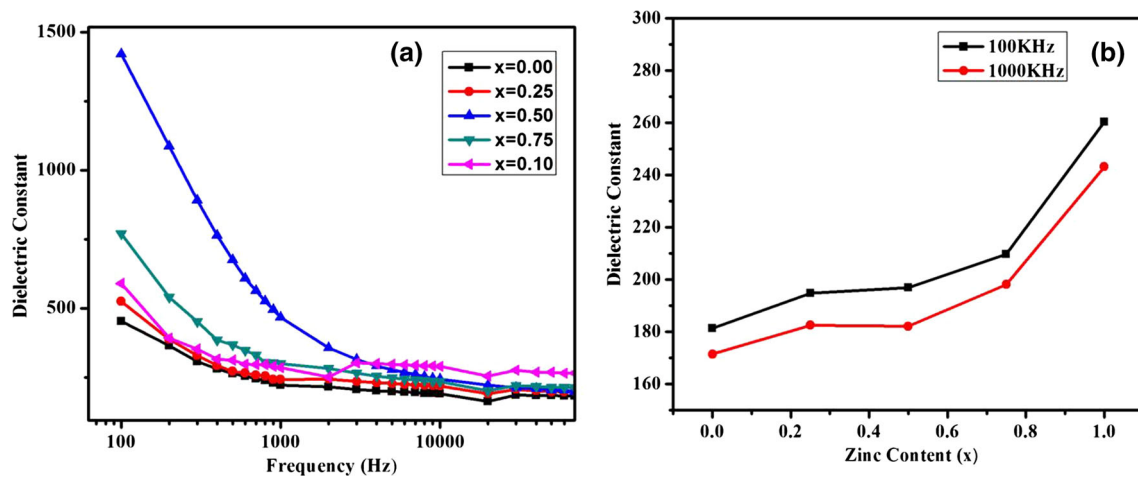**Fig. 6** **a** SEM micrographs. **b** EDAX spectra of $Ni_{1-x}Zn_xFe_2O_4$ (x = 0.0, 0.5 and 1.0)

Fig. 7 a Variation of dielectric constant with frequency. **b** Variation of dielectric constant as a function of zinc content (x) for $Ni_{1-x}Zn_xFe_2O_4$

temperature. The real (ε') and imaginary (ε'') part of dielectric constant, loss tangent (tan δ) were determined from the following relations

$$\varepsilon' = \frac{Cd}{\varepsilon_o A} \qquad (7)$$

$$\varepsilon'' = \varepsilon' \tan \delta \qquad (8)$$

where C is the capacitance of the pellet, d is the thickness of the pellet, A is the cross-sectional area of the flat surface of the pellet and ε_o is the constant of permittivity for free space.

To understand the conduction mechanism, the AC conductivity (σ_{ac}) of the samples was calculated from the values of dielectric constant and dielectric loss factor using the relation

$$\sigma_{ac} = \omega \varepsilon_o \varepsilon' \tan \delta \qquad (9)$$

where ω is the angular frequency.

4.3.1 Variation of dielectric constant (ε') with frequency and Zn concentration (x)

Figure 7a displays the variation of dielectric constant (ε') as a function of frequency at room temperature for the samples $Ni_{1-x}Zn_xFe_2O_4$ (x = 0.0, 0.25, 0.5, 0.75 and 1.0). From Fig. 7a, it is clear that the dielectric constant decreases continuously with increasing frequency and remains almost independent at high frequency region. It is also observed that the dielectric constant decreases steeply at lower frequencies and becomes steady state or constant at higher frequency region. This is normal dielectric behavior of spinel ferrites which is already observed in other nanoferrites at room temperature [29, 30]. This behavior of dielectric constant with frequency can be

explained by Maxwell–Wagner [31, 32] two layers model with Koop's phenomenological theory [33]. In this model, ferrite structure is assumed to consist of good conducting grains separated by poorly conducting intermediate grain boundaries.

The presence of Fe^{3+} and Fe^{2+} ions render ferrite materials to be dipolar. The electron hopping between $Fe^{3+} \leftrightarrow Fe^{2+}$ ions in the ferrite lattice is responsible for dielectric polarization. It is observed that the dielectric constant is a combined effect of dipolar, electronic, ionic and interfacial polarizations. At lower frequency, the dipolar and interfacial polarizations contribute significantly to the dielectric constant. As the frequency increases, ionic and orientation sources of polarizability decreases and finally disappear due to the inertia of the molecules and ions. At higher frequencies, the dielectric constant remains independent of frequency due to the inability of electric dipoles to follow the fast variation of the alternating applied electric field [34].

The variation of dielectric constant (ε') with different Zn concentration for mixed Ni–Zn ferrites at 100 and 1000 kHz frequencies are given in Fig. 7b. This figure shows that the values of dielectric constant is found to increase with increasing Zn content as polarization has largely been attributed to the presence of Fe^{2+} ions which gives rise to heterogeneous spinel structure. Since Fe^{2+} ions are easily polarizable, the larger the number of Fe^{2+} ions, the higher would be the dielectric constant. In Ni–Zn system, Ni ions strongly prefer the occupation of B-sites whereas Zn prefers to go to A-sites. However, Fe ions which exist in $2+$ as well as in $3+$ states, occupy both A and B sites. As Zn substitution increases (at A-sites), replacing Ni ions (at B-sites), some Fe ions will be forced to migrate from A-sites to B-sites. As a result, the number of Fe^{2+} and
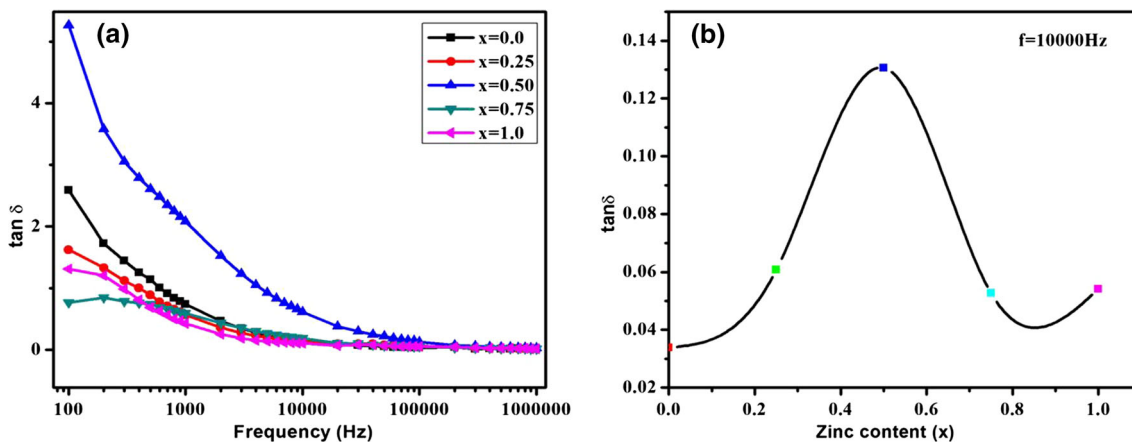
Fig. 8 a Variation of dielectric loss tangent with frequency. **b** Variation of dielectric loss tangent as a function of zinc content (x) for $Ni_{1-x}Zn_xFe_2O_4$

Fe^{3+} ions increases at B-sites while the number of Ni ions decreases as Zn ions substitution increases. As a result, electron hopping between Fe^{3+} and Fe^{2+} ions increases which increases the probability for an electron to reach the grain boundary thus resulting increase in polarization and dielectric constant.

4.3.2 Variation of dielectric loss tangent (tan δ) with frequency and Zn concentration (x)

The values of tan δ depend on a number of factors such as stoichiometry, Fe^{2+} content and structural homogeneity, which in turn depend on the composition of the samples [35]. The variation of dielectric loss tangent for mixed Ni–Zn ferrites at different frequencies at room temperature is shown Fig. 8a. It is observed that the dielectric loss tangent has the same trend as in the case of dielectric

constant. This is due to the fact that at higher frequencies, the domain wall movement is inhibited and magnetization is changed by rotation and hence losses are found to be lower [36]. Similar results have been reported by Ahmed et al. [37] as in the case of nickel ferrite. It can be shown that all the samples show dispersion in tan δ at lower frequencies and particularly predominant at x = 0.5. In this case, the loss factor decreases from 5.27 to 0.026 with the increase in frequency from 100 kHz to 1 MHz as shown in Fig. 8a.

The initial decrease of tan δ with increase in frequency may also be explained on the basis of Koops' phenomenological model [33]. The variation of tan δ with addition of Zn content at 10000 Hz is shown in Fig. 8b. The decrease and then increase in tan δ beyond x = 0.5 may be due to redistribution of cations on tetrahedral (A) and octahedral (B) sites and forming mixed cationic distribution.
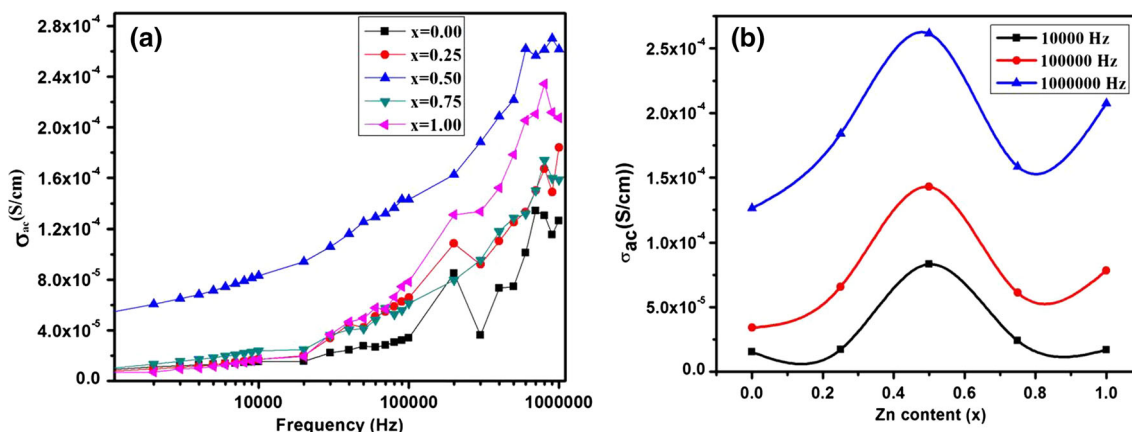

Fig. 9 a Variation of AC conductivity with frequency. **b** Variation of AC conductivity as a function of zinc content (x) for $Ni_{1-x}Zn_xFe_2O_4$

4.3.3 Variation of AC conductivity (σ_{ac}) with frequency on Zn concentration (x)

The conductivity of ferrites, in general, depends on the density, porosity, grain size, grain boundary and chemical composition of the samples [38]. The conduction mechanism and the frequency dependent AC electrical conductivity (σ_{ac}) of nanophase Zn doped nickel ferrites are shown in Fig. 9a.

It is observed that AC conductivity (σ_{ac}) increases with the increase in frequency for all the samples as observed by other worker [39]. It can be explained by the hopping of charge carriers between localized states. It is evident that as the frequency is increased, hopping of the charge carriers is also enhanced, thereby increasing conductivity. Further, at lower frequency, the resistive grain boundaries are more active which act as a hindrance for mobility of charge carriers and hence the hopping of electrons between Fe^{3+} and Fe^{2+} ions is less which is responsible for the slow increase of conductivity. At higher

frequencies, the conductive grains become more active [32] in promoting the hopping of electrons between Fe^{3+} and Fe^{2+} ions and also responsible for creating charger carriers from different centers thereby rapid increase in conductivity.

It is observed from Fig. 9b that σ_{ac} increases with the increase in Zn concentration (x = 0.0 to 0.50) at room temperature. This can be explained by the Verwey and de Boer mechanism [40]. According to El-Sayed [41], the conduction mechanism in Ni–Zn system is a result of electron transfer from Fe^{2+} and Fe^{3+} ions and hole transfer from Ni^{3+} and Ni^{2+} ions at the octahedral (B-sites). On the substitution of zinc in the place of nickel, the hopping of electrons between Fe^{2+} and Fe^{3+} ions on octahedral site increases resulting in the increase of AC conductivity. The increase in conductivity is also due to fact that Zinc has smaller value of resistivity as compared to that of nickel. The decrease and then increase in conductivity beyond x = 0.5 may be due to change in conduction mechanism by means of hopping of holes
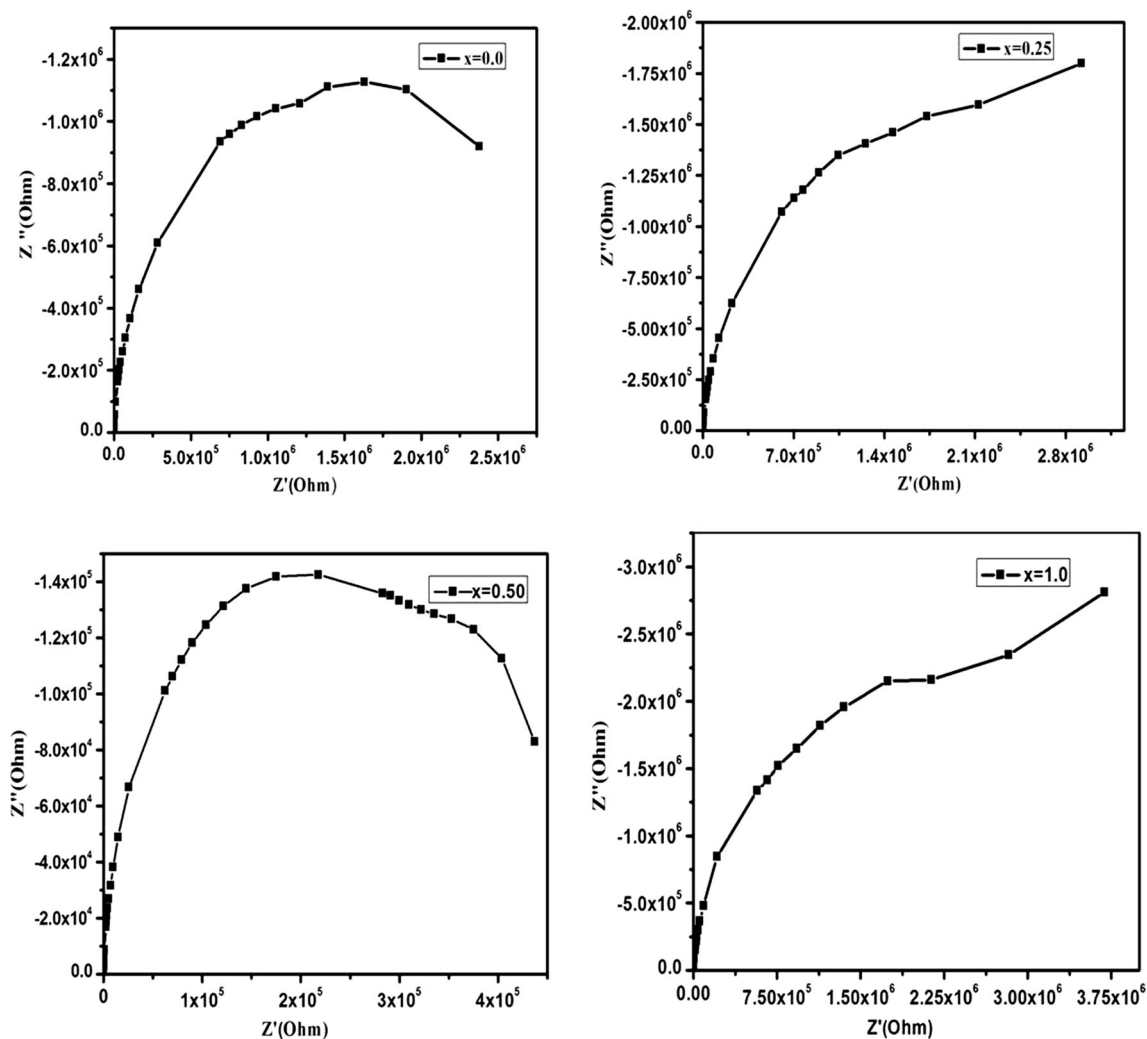

Fig. 10 Cole–Cole plot of $Ni_{1-x}Zn_xFe_2O_4$ (x = 0.0, 0.25, 0.50 and 1.0)

between Ni^{3+} and Ni^{2+} due to redistribution of cations on tetrahedral (A) and octahedral (B) sites and forming mixed cationic distribution.

5 Complex impedance study

In the complex impedance study, the variation of real (Z') and imaginary (Z'') parts of impedance is analyzed by the cole–cole plots (or) Nyquist plots. This plot can be effectively used for complete understanding of the electrical properties of the electro-ceramic materials such as impedance of electrodes, grain and grain boundaries. It also provides the information about the resistive (real part) and reactive (imaginary part) components of a material. A cole–cole plot typically comprises of two successive semicircles. The first semicircle at low frequency is due to the contribution of the grain boundary and second semicircle at high frequency is due to the grain or bulk properties of the materials.

The real and imaginary part of the complex impedance ($Z^*(\omega)$) is given by the following relation

$$Z^*(\omega) = Z'(\omega) + jZ''(\omega) \tag{10}$$

The real (Z') and imaginary part (Z'') of the complex impedance is given by

$$Z' = Z\cos\theta \tag{11}$$

$$Z'' = Z\sin\theta \tag{12}$$

where θ is the phase angle measured by LCR meter.

The Z' data is fit to the equation

$$Z' = \frac{1/R_1}{(1/R_1^2) + \omega^2 C_1^2} + \frac{1/R_2}{(1/R_2^2) + \omega^2 C_2^2} + \frac{1/R_3}{(1/R_3^2) + \omega^2 C_3^2} \tag{13}$$

Single semicircle behavior is usually due to the contribution from the grain or intrinsic bulk contribution (R_1, C_1), whereas, two or more successive semicircles are account of contributions from grain boundary (R_2, C_2) and/or electrodes (R_3, C_3) in a polycrystalline material

Figure 10 shows the room temperature complex impedance or cole–cole plot for the samples $Ni_{1-x}Zn_xFe_2O_4$ with x = 0.0, 0.25, 0.50 and 1.0 as a function of frequency. Two partially overlapping semicircles are found at high and low frequency sides which may be due to the grains and grain boundary effects, respectively. The centers of semicircles are found to lie below the real axis thus indicating a non-Debye type of relaxation process. A sample is assumed to have a microstructure that is made up of parallel conducting plates (grains) separated by resistive plates (grain boundaries). According to the Maxwell–Wagner two layer model, the phenomena is typically related to the existence of a distribution of relaxation time, in which the resulting complex impedance is composed of two overlapping semicircles [42]. The diameter of the semicircles corresponds to the resistance of the grain and grain boundaries. The plot shows that as the Zn concentration increases, the diameter of the semicircle varies indicating the change in resistance of the grain interior and grain boundary.

6 Conclusions

A series of Ni–Zn ferrite with composition $Ni_{1-x}Zn_xFe_2O_4$ (x = 0.0, 0.25, 0.50, 0.75 and 1.0) were prepared using nitrate precursors and urea as the fuel by combustion method. X-ray diffraction measurements confirmed the single phase spinel structure for all the ferrites. The increase in lattice parameter has been observed with increasing Zn concentration in Ni–Zn samples following Vegard's law. The average crystallite size from Scherrer equation is in close agreement with W–H plots. In order to obtain FWHM for both equations, a non-linear least square fit was constructed assuming experimentally obtained X-ray diffraction peaks, obeying Lorentzian function. FTIR was used to identify the formation of Ni–Zn spinel ferrites. EDAX analysis confirms the elemental composition of the synthesized compounds. The dielectric constant and dielectric loss were found to decrease continuously with increasing frequency for all the samples, thus exhibiting the normal dielectric behavior of ferrites. The doping of Zn into $Ni_{1-x}Zn_xFe_2O_4$ has a significant effect on the dielectric constant in the low frequency range, but no pronounced effect was observed at the high frequency region. It is observed that AC conductivity (σ_{ac}) increases with the increase in frequency for all the samples which may be explained on the basis of hopping of charge carriers between localized states. The cole–cole plot shows that as the Zn concentration increases, the diameter of the semicircle varies indicating change in resistance of the grain interior and grain boundary.

References

1. K. Kondo, T. Chiba, S. Yamada, Effect of microstructure on magnetic properties of Ni–Zn ferrites. J. Magn. Magn. Mater. **541**, 254–255 (2003)
2. J. Wang, Prepare highly crystalline NiFe2O4 nanoparticles with improved magnetic properties. Mater. Sci. Eng. B **127**(1), 81–84 (2006)
3. A. Kale, S. Gubbala, R.D.K. Misra, Magnetic behavior of nanocrystalline nickel ferrite synthesized by the revere micelle technique. J. Magn. Magn. Mater. **277**(3), 350–358 (2004)
4. P.Y. Lee, K. Ishizaka, H. Suematsu, W. Jiang, Magnetic and gas sensing property of nanosized NiFe2O4 powders synthesized by pulsed wire discharge. J. Nanopart. Res. **8**(1), 29–35 (2006)

5. K.V.P.M. Shafi, Y. Koltypin, A. Gedanken, R. Prozorov, J. Balogh, J. Lendvai, I. Felner, Sonochemical preparation of nanosized amorphous $NiFe_2O_4$ particles. J. Phys. Chem. B **101**(33), 6409–6414 (1997)

6. D.-H. Chen, X.-R. He, Synthesis of nickel ferrite nanoparticles by sol–gel method. Mater. Res. Bull. **36**(7–8), 1369–1377 (2001)

7. M. Salavati-Niasari, F. Davar, T. Mahmoudi, A simple route to synthesize nanocrystalline nickel ferrite ($NiFe_2O_4$) in the presence of octanoic acid as a surfactant. Polyhedron **28**(8), 1455–1458 (2009)

8. R. Kalai Selvan, C.O. Augustin, L. John Berchmans, R. Saraswathi, Combustion synthesis of $CuFe_2O_4$. Mater. Res. Bull. **38**(1), 41–54 (2003)

9. A. Verma, T.C. Goel, R.G. Mendiratta, M.I. Alam, Dielectric properties of NiZn ferrites prepared by the citrate precursor method. Mater. Sci. Eng. B **60**(2), 156–162 (1999)

10. T. Abraham, Economics of ceramic magnets. Am. Ceram. Soc. Bull. **73**(8), 62 (1994)

11. U.R. Lima, M.C. Nasar, R.S. Nasar, M.C. Rezende, J.H. Araujo, Ni–Zn nanoferrite for radar-absorbing material. J. Magn. Magn. Mater. **320**(10), 1666–1670 (2008)

12. W. Yan, W. Jiang, Q. Zhang, Y. Li, H. Wang, Structure and magnetic properties of nickel–zinc ferrite microspheres synthesized by solvothermal method. Mater. Sci. Eng. B **171**, 144–148 (2010)

13. V. Sreeja, S. Vijayanand, S. Deka, P.A. Joy, Magnetic and Mössbauer spectroscopic studies of NiZn ferrite nanoparticles synthesized by a combustion method. Hyperfine Interact. **183**, 99–107 (2008)

14. S.A. Saafan, T.M. Meaz, E.H. El-Ghazzawy, M.K. El Nimr, M.M. Ayad, M. Bakr, A.C. and D.C. conductivity of NiZn ferrite nanoparticles in wet and dry conditions. J. Magn. Magn. Mater. **322**, 2369–2374 (2010)

15. K. Rama Krishna, K. Vijaya Kumar, D. Ravinder, Structural and electrical conductivity studies in nickel–zinc ferrite. Adv. Mater. Phys. Chem. **2**, 185–191 (2012)

16. M. Zhang, Z. Zi, Q. Liu, P. Zhang, X. Tang, J. Yang, X. Zhu, Y. Sun, J. Dai, Size effects on magnetic properties of $Ni_{0.5}Zn_{0.5}Fe_2O_4$ prepared by sol–gel method. Adv. Mater. Sci. Eng. ID 609819 (2013)

17. A. Hajalilou, M. Hashim, H.M. Kamari, Structure and magnetic properties of $Ni_{0.64}Zn_{0.36}Fe_2O_4$ nanoparticles synthesized by high-energy milling and subsequent heat treatment. J. Mater. Sci. Mater. Electron. **26**(3), 1709–1718 (2015)

18. S. Balaji, R. Kalai Selvan, L. John Berchmans, S. Angappan, K. Subramanian, C.O. Augustin, Combustion synthesis and characterization of Sn^{2+} substituted nonocrystalline $NiFe_2O_4$. Mater. Sci. Eng. B **119**, 119–124 (2005)

19. J. Smit, H.P.J. Wijn, *Ferrites* (Wiley, New York, 1959)

20. P. Scherrer, Gottinger Nachrichten Gesell. **2**, 98 (1918)

21. C.-C. Hwang, J.-S. Tsai, T.-H. Huang, Combustion synthesis of Ni–Zn ferrite by using glycine and metal nitrates—investigations of precursor homogeneity, product reproducibility, and reaction mechanism. Mater. Chem. Phys. **93**(2–3), 330–336 (2005)

22. C. Rath, S. Anand, R.P. Das, K.K. Sahu, S.D. Kulkarni, S.K. Date, N.C. Mishra, Dependence on cation distribution of particle size, lattice parameter and magnetic properties in nanosize Mn–Zn ferrite. J. Appl. Phys. **91**(4), 2211–2215 (2002)

23. S.M. Hoque, Md.A Choudhury, Md. FakhrulIslam, Characterization of Ni–Cu mixed spinel ferrite. J. Magn. Magn. Mater. **251**(3), 292–303 (2002)

24. M. Sorescu, L. Diamandescu, R. Peelamedu, R. Roy, P. Yadoji, Structural and magnetic properties of NiZn ferrites prepared by microwave sintering. J. Magn. Magn. Mater. **279**(2–3), 195–201 (2004)

25. R.D. Waldron, Infrared spectra of ferrites. Phys. Rev. **99**(6), 1727 (1955)

26. P. Priyadharsini, A. Pradeep, P. Sambasiva Rao, G. Chandrasekaran, Structural, spectroscopic and magnetic study of nanocrystalline Ni–Zn ferrites. Mater. Chem. Phys. **116**(1), 207–213 (2009)

27. M. Kaiser, Effect of nickel substitutions on some properties of Cu–Zn ferrites. J. Alloys Compd. **468**(1–2), 15–21 (2009)

28. M. Arshed, M. Siddique, M. Anwar-ul-Islam, N.M. Butt, T. Abbas, M. Ahmed, Site occupancy dependence of magnetism in Ni–Zn ferrites by the Mossbauer effect. Solid State Commun. **93**(7), 599–602 (1995)

29. H.S. Jayanna, B. Nagappa, E. Melagiriyappa, B.J. Madhu, G.D. Prasanna, Dielectric studies on $Mg_xZn_{1-x}Fe_2O_4$ nanoparticles synthesized by combustion method, in *Synthesis and characterization of Nanostructured materials, Macmillan Advanced Research Series*, ed. by V.Rajendran, B.Hillbrands, K.Saminathan, K.E.Geckeler (Macmillan Publishers India Ltd., 2010), pp. 295–298

30. A.T. Raghavender, K.M. Jadhav, Dielectric properties of Al-substituted Co ferrite nanoparticles. Bull. Mater. Sci. **32**(6), 575–578 (2009)

31. J.C. Maxwell, *Electricity and Magnetism*, vol. 1 (Oxford University Press, Oxford, 1929), p. 752

32. K.W. Wagner, Ann. Phys. **40**, 817–855 (1913)

33. C.G. Koops, On the dispersion of resistivity and dielectric constant of some semiconductors at audio frequencies. Phys. Rev. **83**(1), 121–124 (1951)

34. N. Ponpandian, P. Balaya, A. Narayanasamy, Electrical conductivity and dielectric behavior of nanocrystalline $NiFe_2O_4$ - spinel. J. Phys. Condens. Matter **14**(12), 3221–3238 (2002)

35. A. Verma, T.C. Goel, R.G. Mendiratta, P. Kishan, Magnetic properties of nickel–zinc ferrites prepared by the citrate precursor method. J. Magn. Magn. Mater. **208**(1–2), 13–19 (2000)

36. R.A. Andrievski, A.M. Gleze, Size effects in properties of nanomaterials. Scr. Mater. **44**(8–9), 1621–1624 (2001)

37. M.A. Ahmed, E. Ateia, L.M. Salah, A.A. El-Gamal, Structural and electrical studies on La^{3+} substituted Ni–Zn ferrites. Mater. Chem. Phys. **92**(2–3), 310–321 (2005)

38. I.H. Gul, A.Z. Abbasi, F. Amin, M. Anis-ur-Rehman, A. Maqsood, Structural, magnetic and electrical properties of $Co_{1-x}Zn_xFe_2O_4$ synthesized by co-precipitation method. J. Magn. Magn. Mater. **311**(2), 494–499 (2007)

39. S.A. Lokare, R.S. Devan, B.K. Chougule, Structural analysis and electrical properties of ME composites. J. Alloys Compd. **454**(1–2), 471–475 (2008)

40. E.J.W. Verwey, J.H. De Boer, Cations arrangement in a few oxides with crystal structures of the spinel type. Rec. Trav. Chim. Pays Bas **55**, 531–540 (1936)

41. A.M. El-Sayed, Electrical conductivity of nickel–zinc and Cr substituted nickel–zinc ferrites. Mater. Chem. Phys. **82**(3), 583–587 (2003)

42. K.W. Wagner, in *Die Isolierstoffe der Elektrotechnik*, ed. by H. Schering (Springer, Berlin, 1924)